Chemical Science

ROYAL SOCIETY OF CHEMISTRY

EDGE ARTICLE

View Article Online
View Journal | View Issue

Cite this: *Chem. Sci.*, 2025, **16**, 12603

All publication charges for this article have been paid for by the Royal Society of Chemistry

Multilayer graphene crystals with enhanced performances in oxygen reduction and zinc–air batteries *via* interlayer carbon promoted O=O bond dissociation†

Yongfang Qu,‡[ac] Qian Tang,‡[b] Dandan Wang,‡[a] Bing He,*[a] Yong Liu,[c] Wei Chen,[b] Guangtao Yu,*[b] Boyuan Tang,[d] Fujian Liu*[a] and Liangti Qu*[e]

O=O bond activation determines activities of oxygen reduction reaction (ORR) catalysts, and developing metal-free catalysts that outperform precious metals remains challenging. Herein, we demonstrate the mechanochemical polymerization of pyrrole tandem carbonization for designing nitrogen-containing, micropore-penetrated multilayer graphene crystals (NM-MGCs) with abundant barrier-free nanochannels for O_2, leading to high exposure of carbon atoms adjacent to graphitic nitrogen. Due to the ordered multilayer structure with steady layer-by-layer van der Waals interaction, the resultant exposed interlayer carbon atoms exhibit much improved ability to activate O_2 through adsorption-configuration-induced O=O bond dissociation in the ORR with approximately zero energy barrier. Thus, the NM-MGCs show record-breaking ORR performance among metal-free catalysts, which can be fabricated as air cathodes for both flow and flexible Zn–air batteries, exhibiting high maximum power density, high specific capacity (815.30 mA h g_{Zn}^{-1} at 5 mA cm^{-2}), and extraordinary long-term cycling durability (>800 h) and round-trip energy efficiency (63.7%). The overall performance of Zn–air batteries assembled using the NM-MGCs surpass those of commercial Pt/C (20 wt%) and many literature-reported metal and/or metal-free electrocatalysts.

Received 7th April 2025
Accepted 5th June 2025

DOI: 10.1039/d5sc02570b

rsc.li/chemical-science

Introduction

As clean, efficient, and sustainable electrochemical energy storage and conversion devices, metal–air batteries are considered an attractive alternative to traditional fossil fuels, playing pivotal role in meeting energy demands and reducing environmental pollution.[1] Wherein, rechargeable ZABs have garnered significant attention due to their high theoretical specific energy density (1084 W h kg^{-1}), low cost, carbon-free nature, and abundant feedstock reserves.[2] The oxygen reduction reaction (ORR) at the cathode of ZABs primarily relies on platinum-group-metal (PGM)-based catalysts to overcome sluggish kinetics.[3] However, these catalysts suffer from low crustal abundance, high cost, and poor durability. In response, transition metal catalysts (*e.g.*, Fe, Co, and Ni) have been extensively studied, with designed structures such as single-atom metal–nitrogen–carbon showing superior activities in the ORR and ZABs.[4] For practical applications, the challenges of these catalysts such as scale-up synthesis and improvement of anti-sintering and -leaching of metal sites under harsh operating conditions, including high temperature, long-term exposure to strong acid and alkali electrolytes, have not been well tackled yet.[5,6]

Metal-free electrocatalysts offer a promising solution to these issues. Notable examples include heteroatom-doped carbons (*e.g.*, N, P, and S) with versatile architectures,[7] including nanotubes,[8] 2D nanosheets,[9] and 3D porous structures.[10] Specifically, N-doped carbon nanomaterials exhibit good ORR activity, where N atoms could effectively activate adjacent carbon atoms, thus creating abundant catalytically active sites.[11] Increasing the N content has been the primary

[a]*School of Chemistry and Chemical Engineering, Shaoxing University, Shaoxing, 312000, China. E-mail: hebing@usx.edu.cn; fjliu@usx.edu.cn*

[b]*Engineering Research Center of Industrial Biocatalysis, Fujian Provincial Key Laboratory of Advanced Materials Oriented Chemical Engineering, Fujian-Taiwan Science and Technology Cooperation Base of Biomedical Materials and Tissue Engineering, College of Chemistry and Materials Science, Academy of Carbon Neutrality of Fujian Normal University, Fujian Normal University, Fuzhou 350007, China. E-mail: yugt@fjnu.edu.cn*

[c]*Henan Key Laboratory of Polyoxometalate Chemistry, College of Chemistry and Chemical Engineering, Henan University, Kaifeng, 475004, China*

[d]*School of Material Science and Engineering, University of New South Wales, Sydney, New South Wales, 2052, Australia*

[e]*Key Laboratory of Organic Optoelectronics & Molecular Engineering, Ministry of Education, Department of Chemistry, Tsinghua University, Beijing, 100084, China. E-mail: lqu@mail.tsinghua.edu.cn*

† Electronic supplementary information (ESI) available. See DOI: https://doi.org/10.1039/d5sc02570b

‡ These authors contributed equally to this work.

strategy to improve the ORR activity of N-doped carbons. However, the high N-doping level leads to amorphous frameworks with abundant defects, further reducing their long-term stability in the ORR.[12] Additionally, due to the isolated feature of N atoms in the carbon matrix, there is no cooperative interactions between them in the ORR, which results in O=O bond activation that follows a multi-step associative pathway, showing less efficiency compared to high-performance metal catalysts.[13] Hence, rationally regulating the new O=O bond activation pathway on N-doped carbons so as to design efficient metal-free ORR catalysts shows great significance but remains challenging in the field.

Bioinspired by natural systems such as DNA double helix structures, organ self-healing, and artificial polypeptide engineering,[14] the spatial positioning and interatomic interactions of life elements (*e.g.*, N, S, and O) in polymolecular systems greatly affect their aggregated structures,[15] leading to extraordinary functionalities that isolated and disconnected counterparts cannot achieve.[16] This concept has accelerated the development of supramolecular assembly, significantly advancing nanoscience. Manipulation of the spatial position of nitrogen atoms and enhancement of their interactions may present a revolutionary strategy to create highly active sites, which could overcome the limitations of O_2 activation on reported N-doped carbons in the ORR, thus enabling the development of metal-free catalysts that match and/or even outperform PGM catalysts.

Herein, we develop a one-step mechanochemical polymerization tandem carbonization strategy to design high-performance N-containing multilayer graphene crystal-based electrocatalysts (Fig. 1a). The obtained NM-MGCs feature large BET surface areas and graphitized frameworks with micropore-penetrated, highly ordered multilayer structures that serve as barrier-free nanochannels, which are favorable for O_2 to simultaneously interact with the interlayer active carbon atoms adjacent to graphitic-N, exhibiting a unique interlayer synergistic effect due to their steady interlayer van der Waals interactions and suitable lattice distances. The interlayer active carbon atoms, originating from the micropore-penetrated ordered multilayer structure, demonstrated much improved O_2 activation ability in the ORR *via* a unique adsorption-configuration-induced O=O bond dissociative pathway with approximately zero energy barrier, a mechanism not achievable with any other ORR catalysts to date. The NM-MGCs thus showed faster ORR activity than the commercial Pt/C, exhibiting one of the best ORR activities among metal-free catalysts. As a result, NM-MGCs can be further employed as an efficient air cathode for assembling ZABs with both liquid- and solid-state electrolytes, exhibiting excellent overall performances, including impressive maximum power density (221.0 mW cm^{-2}), high specific capacity (815.30 mA h $g_{Zn}{}^{-1}$ at 5 mA cm^{-2}), and extraordinary long-term cycling durability (>800 h) with a round-trip energy efficiency as high as 63.7%. The NM-MGCs also show potential for CO_2 and N_2 electroreduction and could serve as efficient air cathodes in other metal–air batteries.

Results and discussion

NM-MGC preparation and characterization

The NM-MGCs were synthesized through a straightforward mechanochemical process involving the polymerization of pyrrole initiated by $FeCl_3$ without using any solvent, followed by catalytic graphitization of the resulting polypyrrole (ppy) *via* carbonization, and subsequent etching to remove Fe species (Fig. 1a). The NM-MGCs can be easily scaled-up in a kilogram scale (Fig. S1†), giving the yield up to 64.1%, much higher than N-doped porous carbons derived from classical solvent polymerization of the pyrrole tandem carbonization route (Table S1†). Reasonably, the high content of $FeCl_3$ initiator promotes the fast polymerization of pyrrole under solvent free conditions, giving a high polymerization degree and approximately 100% ppy precursor yield. The enhanced coordination interaction between ppy and Fe^{3+} could effectively inhibit the volatilization loss of the ppy precursor and N leaching during carbonization, which result in NM-MGCs with increased product yield in comparison with the literature-reported results.[17]

The framework crystallinity of the NM-MGCs was examined using XRD patterns (Fig. 1b). Notably, NM-MGC-800 and NM-MGC-900 displayed several pronounced and sharp diffraction peaks at approximately 26.3°, 42.2°, 44.3°, 54.5° and 77.5°, corresponding to (002), (100), (101), (004) and (110) planes of standard graphite, respectively, indicating highly graphitized frameworks.[18] In contrast, NM-MGC-700 exhibits broad, low-intensity (002) and (100) diffraction signals, suggesting its poor crystallinity. This observation was further supported by Raman spectroscopy. Two sharp peaks at 1350 cm^{-1} and 1581 cm^{-1}, associated with disordered carbon (D band) and graphitic carbon (G band), were observed in the NM-MGCs (Fig. 1c),[19] and the ratio of I_D/I_G was used to determine their level of graphitization. The I_D/I_G ratios for NM-MGC-700, NM-MGC-800, and NM-MGC-900 were 0.93, 0.76, and 0.71, respectively, indicating that graphitization of NM-MGCs improves with increasing carbonization temperature, consistent with the XRD analysis. The lowest I_D/I_G value of NM-MGC-900 suggests that it has the lowest defect density among the NM-MGCs. Additionally, 2D and S3 signals at 2685 cm^{-1} and 2935 cm^{-1}, particularly evident in NM-MGC-900, further confirm its highly graphitized framework.[20]

The porosity of NM-MGCs was evaluated using N_2 adsorption–desorption isotherms at −196 °C. Besides the high adsorption volume at low pressure ($P/P_0 < 0.1$), the NM-MGCs exhibited typical type IV curves with H3-type hysteresis loops at $P/P_0 = 0.5$–0.95 (Fig. S2a†), indicating the formation of micro-, meso-, and macropores (Table S2†).[21] The pore diameters of NM-MGCs, calculated using the DFT model (Fig. S2b†), ranged from 0.92 to 1.17 nm, confirming the hierarchical porosity within the samples. The BET surface areas and pore volumes of NM-MGCs were in the range of 117–811 $m^2\ g^{-1}$ and 0.02–0.31 $cm^3\ g^{-1}$, respectively, significantly higher than those of many reported graphitized porous carbons.[22–24] Interestingly, both adsorption volumes and BET surface areas of NM-MGCs decreased with increasing carbonization temperature, likely

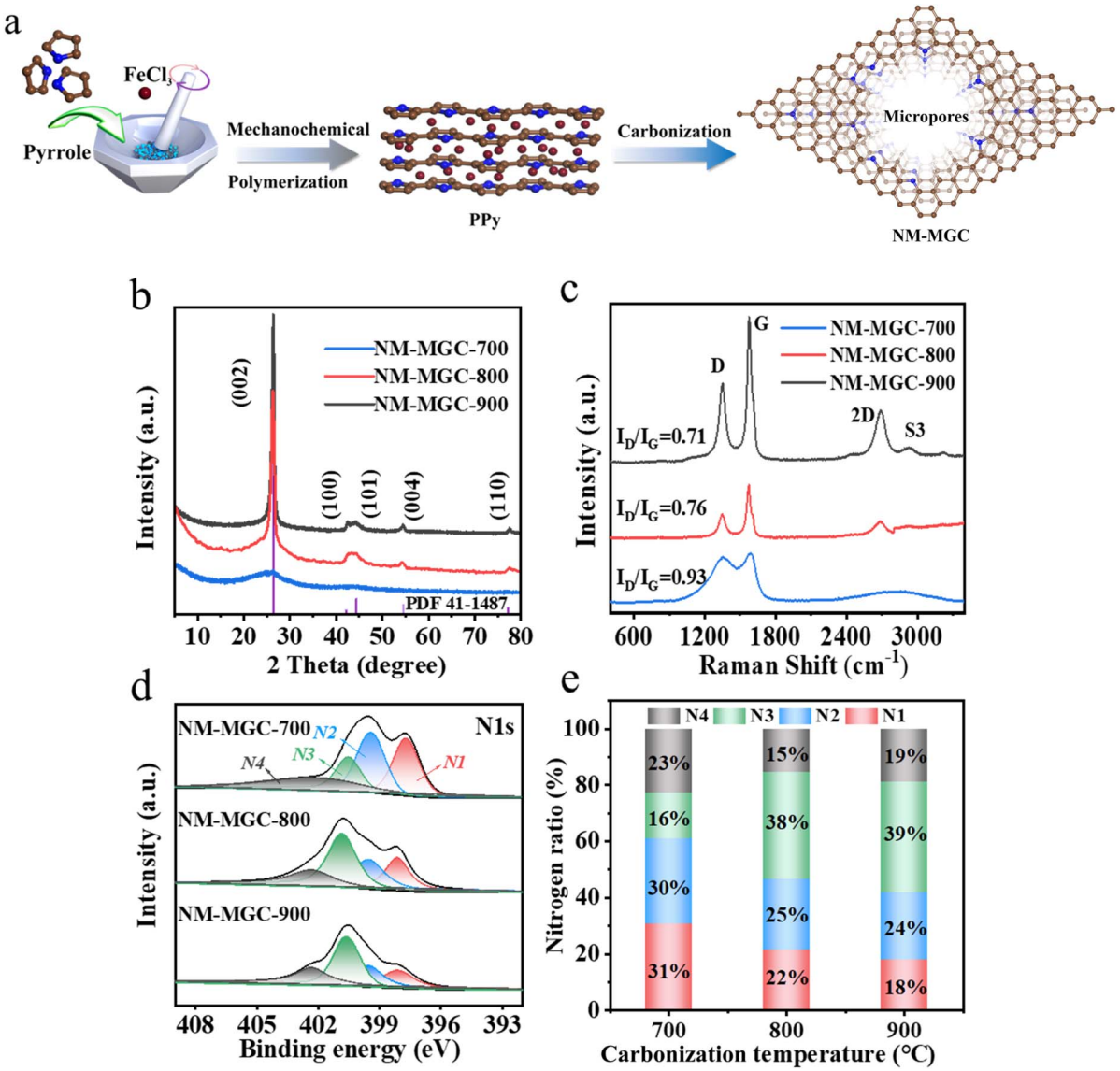

Fig. 1 (a) Synthetic scheme, (b) XRD patterns, (c) Raman spectra, (d) high-resolution N 1s spectra, and (e) nitrogen ratio of NM-MGCs.

due to the graphitization of the framework, which causes pore collapse, framework recombination, and defect reduction. The large BET surface areas and hierarchical porosity provide abundant diffusion channels and facilitate the exposure of inner graphitic-N active sites in various catalytic reactions such as the ORR.

The surface element composition and fine structures of the NM-MGCs were investigated by XPS, showing the signals of C, N and O, but without any Fe residuals (Fig. S3†), which can be further confirmed by ICP-OES results (Table S3†). The C 1s spectra of NM-MGCs can be divided into three peaks at 284.7 eV, 285.8 eV and 288.5 eV, belonging to C–C, C–N and C=O bonds, respectively (Fig. S3b†).[25] The nitrogen contents of NM-MGC-700, NM-MGC-800 and NM-MGC-900 are 7.66 at%, 2.79 at% and 2.34 at%, respectively, which gradually decrease with increasing carbonization temperature. High-resolved N 1s spectra can be divided into four peaks (Fig. 1d) assignable to pyridinic-N (N1, 398.3 eV), pyrrolic-N (N2, 400.1 eV), graphitic-N (N3, 401.1 eV) and oxidized-N (402.8 eV).[26] The pyridinic-N and graphitic-N have been proved to be active sites in oxygen electrocatalysis due to their enhanced abilities to be aware of electronic properties of neighboring carbon atoms, which is beneficial for O_2 adsorption and activation.[27] The ratio of N1 + N3 in NM-MGC-800 (60%) was higher than those in NM-MGC-700 (47%) and NM-MGC-900 (57%, Fig. 1e).

The morphology and internal structures of NM-MGCs were investigated using scanning electron microscopy (SEM), transmission electron microscopy (TEM), and atomic force microscopy (AFM). Notably, 2D nanosheets with a thickness of approximately 4 nm are clearly observable in NM-MGC-800 (Fig. 2a, b and S4†), which are randomly stacked together to form 3D meso–macropores (Fig. 2c).[28] The thickness of the graphite layers at the edge of NM-MGC-800 is around 13 layers, with well-resolved equidistant lattice fringes of crystalline

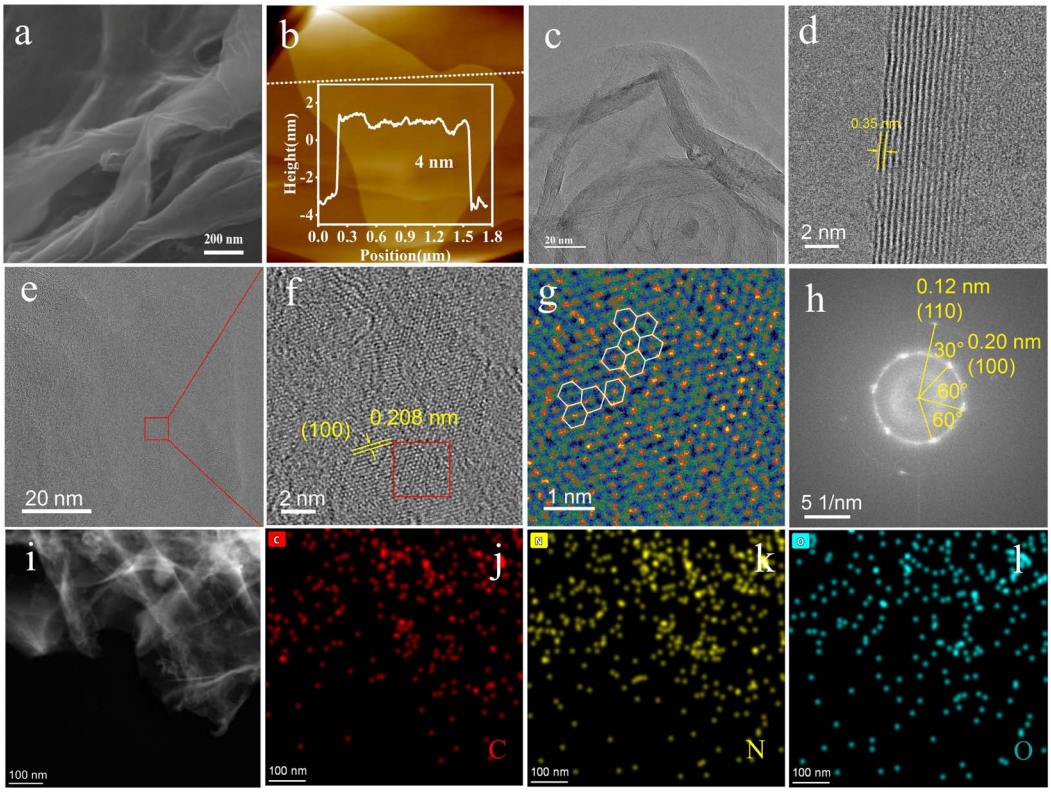

Fig. 2 (a) SEM image; (b) AFM image; (c–e) HRTEM images; (f) magnified image of the marked area in (e); (g) AC-STEM image; (h) SAED image along the [100] zonal axis after FFT; (i) HAADF-STEM image and (j–l) elemental maps of C, N, and O of NM-MGC-800.

carbon, giving interplanar spacings of 0.35 nm and 0.208 nm for the (002) and (100) planes, respectively (Fig. 2d–f). These values show a slight discrepancy from standard graphite (0.337 nm and 0.21 nm) due to nitrogen doping in the graphite lattice of NM-MGC-800, which results in crystal cell distortion. The twisted and deformed hexagonal structural units of the graphitized framework in NM-MGC-800 are further observed in aberration-corrected TEM images (Fig. 2g) after nitrogen atoms are doped into the sample. The highly crystalline framework of NM-MGC-800 is also confirmed by the selective area diffraction pattern derived from the fast Fourier transform (FFT, Fig. 2h).

In addition to stacked meso–macroporous nanochannels, abundant microporous nanochannels penetrate through the interlayer of NM-MGC-800, exhibiting good connectivity and contributing to abundant gas–liquid–solid three-phase interfaces (Fig. S5†). Elemental mapping of NM-MGC-800 shows the even distribution of C, N, and O signals, with a nitrogen doping degree of 3.2 wt% (Fig. 2i–l). These results confirm that the NM-MGCs have highly graphitized frameworks endowed with abundant nitrogen sites. The crystalline framework, tunable nitrogen doping, and versatile micro–meso–macroporous channels improve the stability and provide abundant exposed nitrogen active sites in the NM-MGCs, playing a critical role in its oxygen electrocatalysis properties. The above structural advantages of NM-MGCs should have resulted from their unique synthetic strategy, where strong coordination interaction between ppy and Fe^{3+} formed, further regulating the nitrogen-doping and inducing the formation of micropore-penetrated multilayer structures during carbonization.

Oxygen electrocatalysis

The ORR activities of NM-MGCs were assessed in O_2-saturated 0.1 M KOH solution using a typical three-electrode system. As shown in Fig. S6,† cyclic voltammetry (CV) curves from the ORR display well-defined oxidation peaks for these catalysts. In contrast, no reduction peak was observed in N_2-saturated KOH solution. Notably, NM-MGC-800 exhibited the most positive oxygen reduction peak among the NM-MGCs. The electrocatalytic activities of NM-MGCs were further evaluated using linear sweep voltammetry (LSV) with a rotating disk electrode (RDE) at 1600 rpm (Fig. 3a). NM-MGC-800 exhibited the highest half-wave potential ($E_{1/2}$ = 0.872 V) among NM-MGCs, superior to Pt/C ($E_{1/2}$ = 0.851 V) and many high-performance metal-based electrocatalysts, surpassing any reported metal-free electrocatalysts (Fig. 3b and Table S5†). Meanwhile, NM-MGC-800 presented a comparable onset potential (E_{onset} = 0.996 V) to Pt/C (E_{onset} = 0.995 V). These results demonstrate that NM-MGC-800 possesses impressive ORR performance.

The kinetic properties of various samples in the ORR were studied using Tafel plots. As shown in Fig. 3c, NM-MGC-800 exhibited the fastest reaction kinetics, with a Tafel slope of 79.2 mV dec^{-1}, lower than those of Pt/C (88.9 mV dec^{-1}), NM-MGC-700 (101.8 mV dec^{-1}), and NM-MGC-900 (110.2 mV dec^{-1}). Remarkably, NM-MGC-800 showed favorable ORR

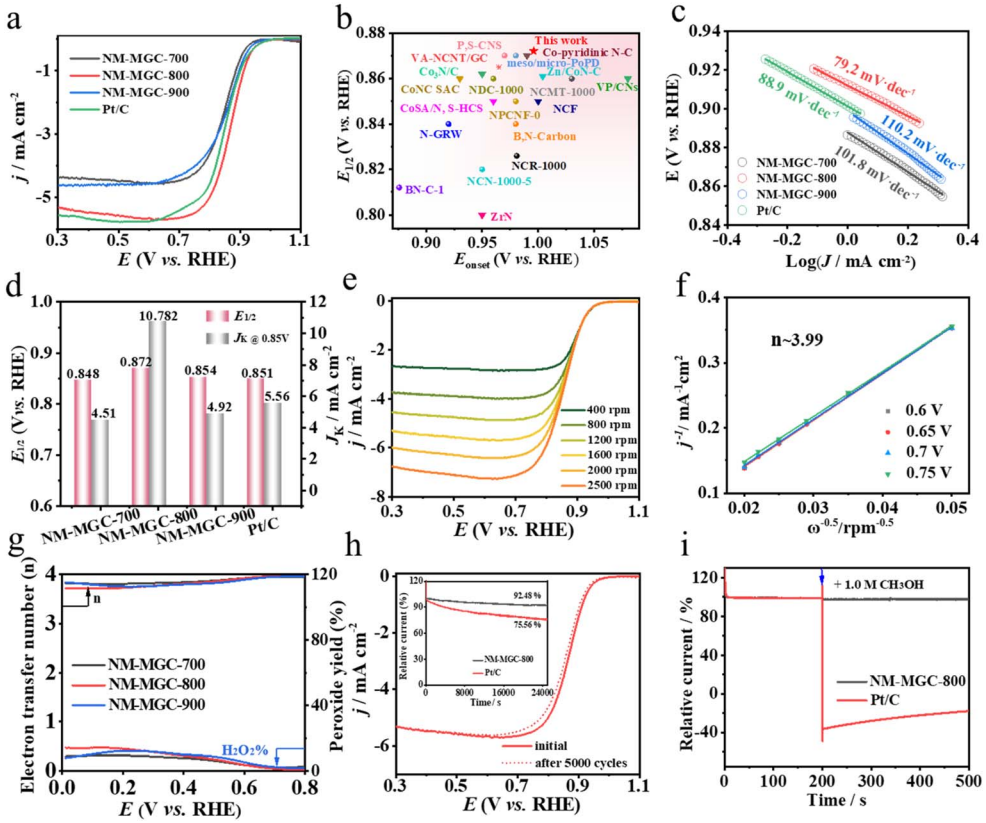

Fig. 3 (a) LSV curves in O_2-saturated 0.1 M KOH on the rotating disk electrode (1600 rpm) of NM-MGCs and Pt/C; (b) comparison of $E_{1/2}$ and E_{onset} of NM-MGC-800 and various reported metal and metal-free electrocatalysts; (c) Tafel slopes and (d) $E_{1/2}$ and J_k @ 0.85 V of NM-MGCs and Pt/C; (e) LSV tests for NM-MGC-800 at different rotational speeds and (f) the related K–L plots (0.6–0.75 V); (g) H_2O_2 yield together with the electron transfer numbers for NM-MGC-800; (h) LSV results for NM-MGC-800 before and after the durability experiment for 5000 cycles in 0.1 M KOH (the inset shows chronoamperometric responses for NM-MGC-800 and Pt/C at 0.4 V); (i) methanol resistance of NM-MGC-800 and Pt/C.

activity, yielding a kinetic current density of 10.782 mA cm^{-2} at 0.85 V, much higher than those of NM-MGC-700 (4.51 mA cm^{-2}), NM-MGC-900 (4.92 mA cm^{-2}), and Pt/C (5.56 mA cm^{-2}) (Fig. 3d). The electron transfer numbers (n) of the NM-MGCs were determined from Koutecky–Levich (K–L) plots obtained from LSVs at various rotation speeds (Fig. 3e and S7†).[29] Fig. 3f and S7† show nearly linear K–L plots for NM-MGCs at various potentials, indicating first-order kinetics with respect to dissolved oxygen concentration.[30] The n value of NM-MGCs was approximately 4, calculated from K–L plots, indicating that NM-MGCs primarily undergo a direct four-electron transfer pathway in the ORR.

The ORR pathway was further examined using rotating ring-disk electrode (RRDE) measurements (Fig. S8†). As shown in Fig. 3g, NM-MGC-800 displayed an ideal four-electron reaction mechanism with the lowest peroxide yield, below 8%, in the potential range of 0.2–0.8 V, indicating higher OH^- selectivity. Apart from activity, stability and methanol tolerance are crucial for practical applications, which were assessed using chronoamperometry tests. NM-MGC-800 retained 92.48% of its original current after 25 000 s of chronoamperometry, significantly better than the 75.56% retention of Pt/C (Fig. 3h). Additionally, NM-MGC-800 showed no reduction in half-wave potential or limited current density after 5000 continuous CV cycles (Fig. 3h). In contrast, the half-wave potential of Pt/C decreased by about 28 mV (Fig. S9†). Furthermore, the current of NM-MGC-800 remained almost unchanged after the injection of 1.0 M methanol at 200 s, while Pt/C showed significant reduction due to methanol poisoning (Fig. 3i). These results demonstrate the superior stability and methanol resistance of NM-MGC-800 in the ORR.

From the ORR half-wave potential to the OER overpotential at 10 mA cm^{-2}, NM-MGC-800 shows an E_{gap} of 0.660 V, lower than those of the combination of Pt/C and RuO_2 (0.664 V), NM-MGC-700 (0.788 V), and NM-MGC-900 (0.888 V), and much lower than those of many reported metal- or metal-free catalysts in the literature (Fig. S10a and b, Table S4†). Electrochemical impedance spectroscopy (EIS) was used to gain insight into the kinetics of NM-MGCs. NM-MGC-800 exhibits the smallest semicircle diameter among the NM-MGCs, indicating the lowest electrochemical charge transfer resistance, which confirms faster charge transfer at the multi-scaled interface of NM-MGC-800 (Fig. S11a†). The superior hydrophilicity of NM-MGC-800 is beneficial for increasing the reaction interface, further boosting the electrocatalytic reaction efficiency (Fig. S11b†). These results confirm that NM-MGC has great

potential for sustainable energy devices. The excellent ORR performances and long-term stability of NM-MGCs are determined by their stable graphitized frameworks, barrier-free diffusion channels, and abundant and highly exposed carbon aggregate active sites.

Application of NM-MGC in ZABs

Given the superior performance of NM-MGCs in oxygen electrocatalysis, we explored their application in ZABs. A primary ZAB was fabricated using NM-MGC-800 and Pt/C loaded on carbon paper as air cathode materials, with a polished Zn plate as the anode and a mixed solution of 6 M KOH + 0.2 M $Zn(OAc)_2$ as the electrolyte (Fig. 4a). Detailed testing procedures and battery assembly are described in the ESI.† The open-circuit voltage of the battery assembled with NM-MGC-800 reached 1.464 V, which is higher than that of the Pt/C catalysts (1.431 V, Fig. 4b). According to the discharge polarization and power density curves (Fig. 4c), NM-MGC-800 exhibited superior discharge performance, giving a high maximum power density of 221.0 mW cm^{-2}, far beyond that of Pt/C (177.2 mW cm^{-2}) and mostly reported metal- or metal-free catalysts (Table S6†).

From the galvanostatic discharge curves (Fig. 4d), the NM-MGC-800-based ZABs delivered higher current densities than those with Pt/C catalysts. Notably, the reversible discharge

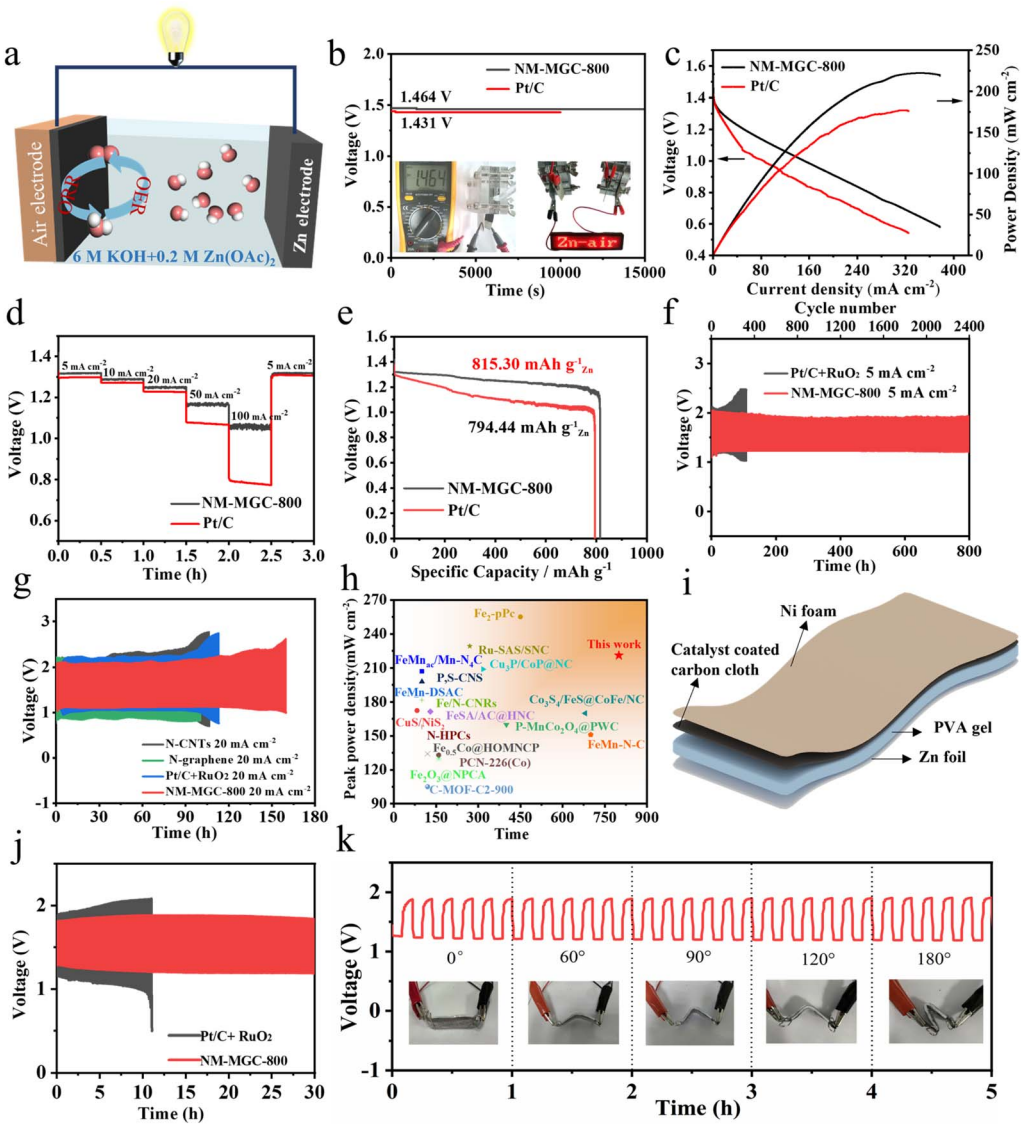

Fig. 4 (a) Diagram of self-assembled ZABs; (b) open circuit potential (the inset shows photographs of a multipurpose meter and an LED indicator powered by NM-MGC-800-based ZABs); (c) power density curves; (d) galvanostatic discharge curves at various current densities; (e) galvanostatic discharge curves at 5 mA cm^{-2}; (f) discharge–charge cycling curves at 5 mA cm^{-2}; (g) discharge–charge cycling curves of N-CNTs, N-graphene, Pt/C + RuO_2 and NM-MGC-800 at 20 mA cm^{-2}; (h) comparison of discharge–charge durability and peak power density of NM-MGC-800 and various reported ZABs; (i) scheme of quasi-solid-state flexible ZABs; (j) discharge–charge cycling curves at 2 mA cm^{-2} of NM-MGC-800 and Pt/C + RuO_2-based quasi-solid-state flexible ZABs; (k) cycling performance curves at 2 mA cm^{-2} of NM-MGC-800-based quasi-solid-state flexible ZABs in different bending states.

capacity remained stable when the current density was returned to 5 mA cm^{-2}, indicating significant rate capability and good reversibility of the NM-MGC-800 cathode. Moreover, an impressive specific capacity of 815.30 mA h g_{Zn}^{-1} at 5 mA cm^{-2} was achieved on NM-MGC-800, normalized to the amount of Zn, which is significantly higher than that of ZABs based on Pt/C (794.44 mA h g_{Zn}^{-1}, Fig. 4e).

To further assess the cycling stability of the NM-MGC-800-based ZABs, we conducted galvanostatic discharge–charge performance tests at 5 mA cm^{-2} for 2400 cycles over 800 h (10 min per cycle). The initial discharge/charge voltage gap was 0.68 V for the NM-MGC-800-based ZABs, with a high round-trip energy efficiency of up to 61.5%. This efficiency remained stable with a high energy retention of 63.7% even for 800 h of operation. In contrast, ZABs based on Pt/C + RuO_2 showed significant voltage attenuation, with the discharge–charge voltage gap widening from 0.6 V to 0.8 V after just 100 h of continuous operation, and the round-trip energy efficiency decreasing from 60% to 50% (Fig. 4f and S12†), demonstrating the inefficiency of Pt/C + RuO_2 catalysts in sustaining discharge–charge cycles.

Even at a higher current density of 20 mA cm^{-2}, the NM-MGC-800-based ZABs exhibited smaller discharge–charge voltage gaps over 360 cycles in 120 h, outperforming N-CNTs, N-graphene, and Pt/C + RuO_2 catalysts (Fig. 4g). This superior performance is attributed to the exceptional oxygen electrocatalysis of NM-MGC-800. Although the discharge/charge voltage gap gradually widened at higher current densities of 30 and 50 mA cm^{-2}, the NM-MGC-800-based ZABs still maintained steady performance at 50 mA cm^{-2} for 19 h over 57 cycles (Fig. S13†) due to its superior activity and outstanding stability in oxygen electrocatalysis. The property degradation of the assembled ZABs at higher current densities was primarily due to the formation of Zn dendrites. Overall, the NM-MGC-800-based ZABs show outstanding overall performance and record-breaking discharge/charge stability to date (Fig. 4h).

Flexible ZABs have garnered significant research interest due to their potential as green, efficient, and sustainable power sources, particularly for use in portable and wearable electronics. To explore this application, NM-MGC-800 was employed as the air cathode in the assembly of flexible ZABs. A sandwich-type quasi-solid-state flexible ZAB was constructed using a self-standing NM-MGC-800 cathode, an alkaline poly(-vinyl alcohol) (PVA) gel electrolyte, a Zn foil anode, and a nickel foam current collector (Fig. 4i). The NM-MGC-800-based ZABs exhibited a lower voltage gap between the charge and discharge plateaus compared to Pt/C + RuO_2 catalysts. It delivered a maximum power density of 85 mW cm^{-2}, significantly higher than the 37 mW cm^{-2} achieved by the Pt/C + RuO_2 catalysts (Fig. S14†).

Notably, NM-MGC-800 demonstrated superior long-term galvanostatic discharge and charge performance at a current density of 2 mA cm^{-2}. Stable charge and discharge voltages of 1.82 V and 1.28 V, respectively, were maintained over 30 h and 180 cycles (5 minutes per cycle), resulting in a high round-trip energy efficiency of up to 70% (Fig. 4j). In contrast, the Pt/C + RuO_2 catalysts exhibited a significant voltage drop, with their discharge and charge voltages deteriorating from 1.15 V and 1.89 V to 0.5 V and 2.07 V, respectively, after only 66 cycles, leading to a marked decrease in round-trip energy efficiency from 60.8% to 24.2%. Furthermore, the quasi-solid-state ZABs with NM-MGC-800 displayed stable discharge and charge voltages even under mechanical bending from 0° to 180° over 5 hours of operation (Fig. 4k). This stability under mechanical stress suggests that NM-MGC-800 is a promising candidate for use in flexible and safe energy storage devices.

Understanding extremely high ORR performance of NM-MGCs

To gain deeper insights into the exceptional ORR activity of NM-MGC-800 in ZABs, DFT calculations were performed. Based on structural characterization, a theoretical model was constructed by stacking two N-doped graphene layers with a large hole, incorporating representative N-doping modes: graphitic-N, pyridinic-N, and pyrrolic-N (Fig. 5a and S15†). The calculations reveal that two oxygen atoms in O_2 preferentially interact with two carbon atoms situated in different graphene layers adjacent to graphitic-N (Fig. S16†). The corresponding adsorption energy (ΔE_{O_2}) is approximately zero (0.05 eV), indicating an optimal adsorption state for O_2. This suggests that carbon atoms adjacent to graphitic-N (denoted as C_{gN}) serve as the ideal sites for O_2 adsorption, facilitating the subsequent ORR process.

Further charge density difference ($\Delta\rho$) calculations indicate significant electron transfer during the interaction of O_2 with C_{gN} sites (Fig. 5b). Specifically, up to 1.08$|e|$ is transferred from the graphene layers to the adsorbed O_2, as shown by the calculated Bader charge. This electron transfer occupies antibonding π-orbitals of the adsorbed O_2 molecule, leading to significant extension of the O–O bond length from 1.23 Å to 1.52 Å. Additionally, the calculated distances between the carbon and oxygen atoms range from 1.42 to 1.44 Å, indicating the formation of two C–O bonds. Partial density of states (PDOS) analysis supports these findings, showing significant hybridization between O 2p and C 2p orbitals (Fig. 5c). These results suggest that O_2 can be effectively activated and prefers to dissociate into two O* species due to the synergistic effects of the C atoms adjacent to graphitic-N in different graphene layers.

Encouragingly, the calculations show a near-zero energy barrier for the dissociation of O_2 into O* + O* (Fig. S17†), indicating the favorable kinetics. This dissociation process is also exothermic, releasing approximately 0.34 eV of heat, making it thermodynamically favorable as well. Obviously, the dissociation mechanism will dominate the ORR process on our catalyst. This contrasts with the higher energy barriers seen in other material systems, such as 2D PtTe (0.32 eV),[31] B-doped Pd (111) (0.63 eV),[32] and even Pt (111) (0.48 eV).[33] For the subsequent reduction step from O* + O* to O* + OH*, two reaction paths were considered, referred to as paths I and II, corresponding to different graphene layers where the O* species reside. Remarkably, all reaction steps proceed energetically downhill, with the fourth thermodynamic step ($OH^* \rightarrow {}^*+H_2O$), serving as the potential-determining step (PDS) in both paths I and II (Fig. 5d). The calculated overpotentials (η) are as low as

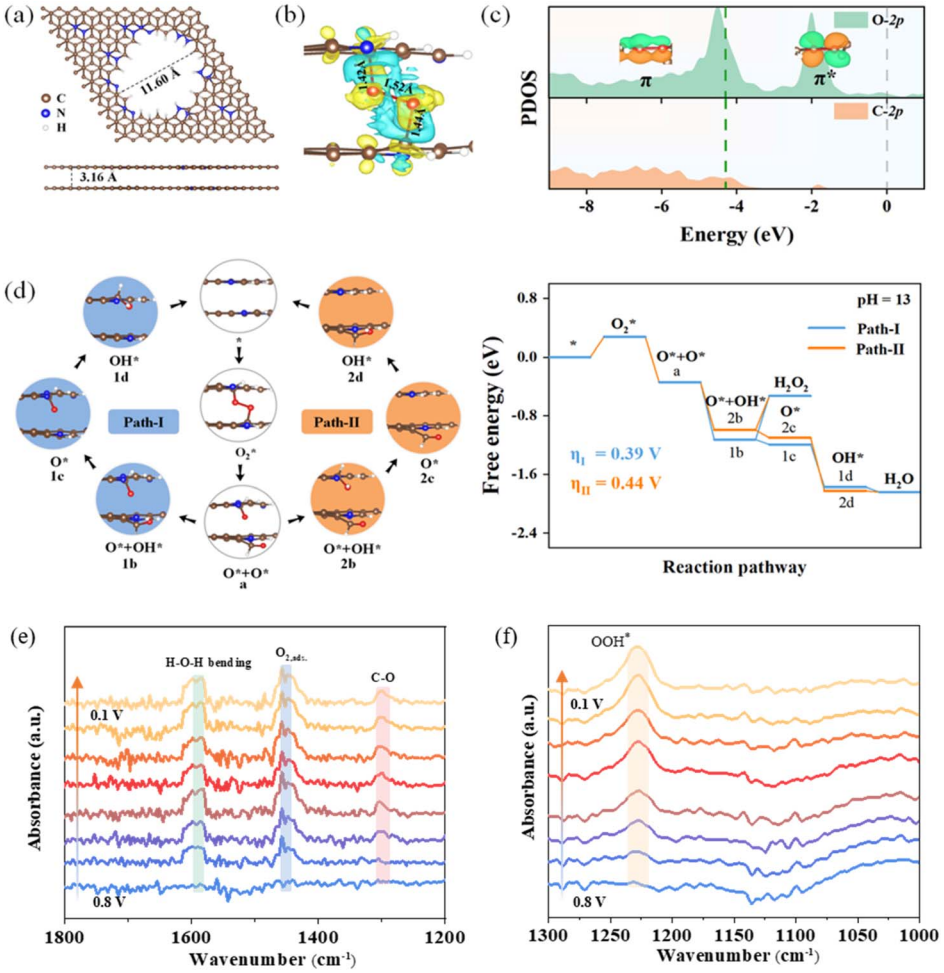

Fig. 5 (a) The bilayer N-doped graphene model. (b) The charge difference distribution ($\Delta\rho$) of O_2 adsorbed on the two C atoms adjacent to graphitic-N atoms located in different graphene layers. (c) Partial density of states (PDOSs) of O_2 adsorbed on the C atoms that are neighbors to graphitic-N atoms located in different graphene layers. The Fermi level is set to zero (gray dash line). Inset: the molecular orbitals of the adsorbed O_2 in different energy ranges marked by green dash lines. (d) The Gibbs free energy diagrams of the ORR on the relevant C atoms adjacent to graphitic-N. (e and f) *In situ* FTIR spectra of NM-MGC-800 and NM-MGC-700 during the ORR in 0.1 M KOH.

0.39 V for path I and 0.44 V for path II, which are lower than those reported for N-graphene systems (0.60–0.75 V)[19,26,34] and even lower than Pt (111) (0.45 V),[35] indicating the excellent ORR performance of NM-MGC-800.

Moreover, the calculations show that the association ORR pathway on NM-MGC-800 cannot proceed as the intermediate OOH* dissociates into O* and OH*, further confirming that the dissociation mechanism mainly dominates the ORR process. This quite differs from previously reported N-doped graphene ORR electrocatalysts,[19,26,34] where the associative mechanism is more common. Additionally, the formation of H_2O_2 as a by-product is highly endothermic (Fig. 5d), suggesting that the four-electron dissociation pathway effectively suppresses the two-electron pathway, leading to high reaction selectivity.

Experimental verification of the DFT results was carried out by using O_2-temperature programmed desorption mass spectrometry (O_2-TPD-MS), O_2 adsorption isotherm measurements and *in situ* infrared spectroscopy. Notably, NM-MGCs showed much enhanced O_2 capacities than those of graphene and N-doped graphene without micropores, which indicates that micropores play a key role in their enrichment and storage of O_2. Additionally, NM-MGC-800 and -900 exhibited much stronger O_2 desorption peaks at high temperatures compared to NM-MGC-700, N-doped graphene and N-CNTs. These phenomena suggest that the enhanced interaction between O_2 and NM-MGC-800 and -900, resulting from their ordered multi-layered graphitized network, can enable the micropore stored O_2 to be firmly fixed at the intersection of ordered graphite layers and micropores (Fig. S18†).

In situ infrared spectroscopy of NM-MGC-800 revealed signals at 1450 cm^{-1} and 1580 cm^{-1}, corresponding to the O–O stretching mode of adsorbed O_2 and water formed during the ORR (Fig. 5e). Notably, a peak at 1228 cm^{-1}, associated with OOH*, emerged over time in NM-MGC-700 with a disordered interlayer structure (Fig. 5f), indicating that the associative pathway dominates the ORR.[36–38] The absence of OOH* and the presence of a new peak at 1297 cm^{-1}, corresponding to the C–O bond in NM-MGC-800, confirm that the O=O bond

dissociation pathway plays a main role in the ORR. This process releases O* intermediates, which strongly interact with the active carbon atoms adjacent to the edge of graphitic-N to form C–O bonds due to their unique electron donor–acceptor interaction. These findings align well with the DFT calculations and O_2-TPD-MS results, indicating that NM-MGC-800 is highly conducive to O_2 adsorption and activation, significantly promoting the ORR through O=O bond dissociation, thus achieving extremely high ORR activity and OH^- selectivity.

Conclusions

We have developed a mechanochemical polymerization tandem carbonization methodology for designing N-containing multilayer graphene crystals, with abundant micropores penetrating through the ordered graphite layers, serving as barrier-free nanochannels for O_2 diffusion. Efficient activation of interlayer carbon atoms by the adjacent graphitic-N nearby the microporous channels was achieved on NM-MGCs. The resultant exposed interlayer active carbon atom aggregates show enhanced ability to activate O_2 in the ORR *via* adsorption-configuration-induced O=O bond dissociation with approximately zero energy barrier. As a result, the NM-MGCs exhibit superior ORR activity to commercial Pt/C, achieving record-high performance among N-doped carbons. The NM-MGCs were further employed as an efficient air cathode for rechargeable ZABs with both liquid- and solid-state electrolytes, and their power density, specific capacity, cycling durability, and round-trip energy efficiency were better than those of Pt-tandem Ru-catalysts and almost all literature-reported metal-free catalysts. This work provides new opportunities for the development of efficient and durable carbon-based oxygen electrocatalysts, offering valuable insights for the design of advanced carbon energy materials in the future.

Data availability

The data that support the findings of this study are available from the corresponding author upon reasonable request.

Author contributions

Yongfang Qu, Qian Tang and Dandan Wang: writing – original draft, data curation, methodology. Bing He: supervision, validation, conceptualization. Yong Liu: project administration, validation. Wei Chen and Guangtao Yu: funding acquisition, supervision, theoretical calculations. Boyuan Tang: writing – review & editing, validation. Fujian Liu: funding acquisition, writing – review & editing, conceptualization, supervision. Liangti Qu: writing – review & editing, supervision.

Conflicts of interest

The authors declare no competing financial interest.

Acknowledgements

This work was supported by the National Natural Science Foundation of China (22005192, 21573150, and 22473026). We also gratefully acknowledge support from the Natural Science Foundation of Fujian Province (2024J011012, 2022J01167 and 2024J01289), the Research Funding of the Academy of Carbon Neutrality at Fujian Normal University (TZH2022-05), the Minjiang Scholar Program, and the startup fund for high-level talent at Fujian Normal University. Additionally, we thank the Fujian-Taiwan Science and Technology Cooperation Base of Biomedical Materials and Tissue Engineering (2021D039) for their support. We extend our appreciation to the Computing Center of Jilin Province for providing supercomputer time.

Notes and references

1 J. Liu, Y. Liu, N. Liu, Y. Han, X. Zhang, H. Huang, Y. Lifshitz, S.-T. Lee, J. Zhong and Z. Kang, *Science*, 2015, **347**, 970–974.
2 W. Sun, F. Wang, B. Zhang, M. Zhang, V. Kuepers, X. Ji, C. Theile, P. Bieker, K. Xu, C. Wang and M. Winter, *Science*, 2021, **371**, 46–51.
3 K. Cui, X. Tang, X. Xu, M. Kou, P. Lyu and Y. Xu, *Angew. Chem., Int. Ed.*, 2024, **63**, e202317664.
4 W. Yan, W. Chen and Y. Chen, *Adv. Funct. Mater.*, 2024, **34**, 2401027.
5 S. Unsal, R. Girod, C. Appel, D. Karpov, M. Mermoux, F. Maillard, V. A. Saveleva, V. Tileli, T. J. Schmidt and J. Herranz, *J. Am. Chem. Soc.*, 2023, **145**, 7845–7858.
6 S. Zhang, Y. Han, X.-Y. Li, Q. Tang, B. Zhu and Y. Gao, *J. Am. Chem. Soc.*, 2025, **147**, 15796–15805.
7 P. Cui, L. Zhao, Y. Long, L. Dai and C. Hu, *Angew. Chem., Int. Ed.*, 2023, **62**, e202218269.
8 G. Chen, Y. Liu, S. Xue, R. Zhang, H. Lv, J. Zhang, L. Wu and R. Che, *Small*, 2024, **20**, 2308192.
9 Z. Xiang, D. Cao, L. Huang, J. Shui, M. Wang and L. Dai, *Adv. Mater.*, 2014, **26**, 3315–3320.
10 Y. Qiao, P. Yuan, Y. Hu, J. Zhang, S. Mu, J. Zhou, H. Li, H. Xia, J. He and Q. Xu, *Adv. Mater.*, 2018, **30**, 1804504.
11 D. Guo, R. Shibuya, C. Akiba, S. Saji, T. Kondo and J. Nakamura, *Science*, 2016, **351**, 361–365.
12 H. B. Yang, J. Miao, S.-F. Hung, J. Chen, H. B. Tao, X. Wang, L. Zhang, R. Chen, J. Gao, H. M. Chen, L. Dai and B. Liu, *Sci. Adv.*, 2016, **2**, e1501122.
13 Y. Zeng, C. Li, B. Li, J. Liang, M. Zachman, D. Cullen, R. Hermann, E. E. Alp, B. Lavina, S. Karakalos, M. Lucero, B. Zhang, M. Wang, Z. Feng, G. Wang, J. Xie, D. Myers, J.-P. Dodelet and G. Wu, *Nat. Catal.*, 2023, **6**, 1215–1227.
14 N. Akter, B. S. Alladin-Mustan, Y. Liu, J. An and J. M. Gibbs, *J. Am. Chem. Soc.*, 2024, **146**, 18205–18209.
15 S. Chen, L. Lee, T. Naila, S. Fishbain, A. Wang, A. E. Tomkinson, S. P. Lees-Miller and Y. He, *Nature*, 2021, **593**, 294–298.
16 R. Li, Y. Zhu, X. Gong, Y. Zhang, C. Hong, Y. Wan, X. Liu and F. Wang, *J. Am. Chem. Soc.*, 2023, **145**, 2999–3007.

17 N. Zheng, X. Zhang, C. Zhang, X. Hu, J. Pan, C. Wu, Y. He, X. Zhang, L. Dong, Y. Yu and W. Liu, *Matter*, 2022, **5**, 1603–1615.
18 C. Tsounis, B. Subhash, P. V. Kumar, N. M. Bedford, Y. Zhao, J. Shenoy, Z. Ma, D. Zhang, C. Y. Toe, S. Cheong, R. D. Tilley, X. Lu, L. Dai, Z. Han and R. Amal, *Adv. Funct. Mater.*, 2022, **32**, 2203067.
19 H. Jiang, J. Gu, X. Zheng, M. Liu, X. Qiu, L. Wang, W. Li, Z. Chen, X. Ji and J. Li, *Energy Environ. Sci.*, 2019, **12**, 322–333.
20 L.-J. Yuan, B. Liu, L.-X. Shen, Y.-K. Dai, Q. Li, C. Liu, W. Gong, X.-L. Sui and Z.-B. Wang, *Adv. Mater.*, 2023, **35**, 2204031.
21 Y.-X. Zhao, J.-H. Wen, P. Li, P.-F. Zhang, S.-N. Wang, D.-C. Li, J.-M. Dou, Y.-W. Li, H.-Y. Ma and L. Xu, *Angew. Chem., Int. Ed.*, 2023, **62**, e202216950.
22 Z. Lyu, S. Yu, M. Wang, P. Tieu, J. Zhou, Q. Shi, D. Du, Z. Feng, X. Pan, H. Lin, S. Ding, Q. Zhang and Y. Lin, *Small*, 2024, **20**, 2308278.
23 B. Cao, Q. Zhang, H. Liu, B. Xu, S. Zhang, T. Zhou, J. Mao, W. K. Pang, Z. Guo, A. Li, J. Zhou, X. Chen and H. Song, *Adv. Energy Mater.*, 2018, **8**, 1801149.
24 T. Sun, W. Zang, H. Yan, J. Li, Z. Zhang, Y. Bu, W. Chen, J. Wang, J. Lu and C. Su, *ACS Catal.*, 2021, **11**, 4498–4509.
25 C. Sun, J. Ding, H. Wang, J. Liu, X. Han, Y. Deng, C. Zhong and W. Hu, *J. Mater. Chem. A*, 2021, **9**, 13926–13935.
26 F. Kong, X. Cui, Y. Huang, H. Yao, Y. Chen, H. Tian, G. Meng, C. Chen, Z. Chang and J. Shi, *Angew. Chem., Int. Ed.*, 2022, **61**, e202116290.
27 K. Wu, L. Zhang, Y. Yuan, L. Zhong, Z. Chen, X. Chi, H. Lu, Z. Chen, R. Zou, T. Li, C. Jiang, Y. Chen, X. Peng and J. Lu, *Adv. Mater.*, 2020, **32**, 2002292.
28 Z. Zhan, J. Yu, S. Li, X. Yi, J. Wang, S. Wang and B. Tan, *Small*, 2023, **19**, 2207646.
29 X. Tian, X. Zhao, Y.-Q. Su, L. Wang, H. Wang, D. Dang, B. Chi, H. Liu, E. J. M. Hensen, X. W. Lou and B. Y. Xia, *Science*, 2019, **366**, 850–856.
30 X. Xie, H. Peng, K. Sun, W. Li, A. Liang, G. Ma, Z. Lei and Y. Xu, *Adv. Funct. Mater.*, 2024, **34**, 2316037.
31 Y. Wang, Y. Li and T. Heine, *J. Am. Chem. Soc.*, 2018, **140**, 12732–12735.
32 T. T. Vo Doan, J. Wang, K. C. Poon, D. C. L. Tan, B. Khezri, R. D. Webster, H. Su and H. Sato, *Angew. Chem., Int. Ed.*, 2016, **55**, 6842–6847.
33 R. Jinnouchi, K. Kodama, T. Suzuki and Y. Morimoto, *J. Chem. Phys.*, 2015, **142**, 184709.
34 J. Gao, Y. Wang, H. Wu, X. Liu, L. Wang, Q. Yu, A. Li, H. Wang, C. Song, Z. Gao, M. Peng, M. Zhang, N. Ma, J. Wang, W. Zhou, G. Wang, Z. Yin and D. Ma, *Angew. Chem., Int. Ed.*, 2019, **58**, 15089–15097.
35 J. K. Norskov, J. Rossmeisl, A. Logadottir, L. Lindqvist, J. R. Kitchin, T. Bligaard and H. Jónsson, *J. Phys. Chem. B*, 2004, **108**, 17886–17892.
36 S. Mondal, D. Bagchi, M. Riyaz, S. Sarkar, A. K. Singh, C. P. Vinod and S. C. Peter, *J. Am. Chem. Soc.*, 2022, **144**, 11859–11869.
37 Z. Huang, M. Li, X. Yang, T. Zhang, X. Wang, W. Song, J. Zhang, H. Wang, Y. Chen, J. Ding and W. Hu, *J. Am. Chem. Soc.*, 2024, **146**, 24842–24854.
38 H. Xia, R. Pang, X. Dong, Q. Liu, J. Chen, E. Wang and J. Li, *J. Am. Chem. Soc.*, 2023, **145**, 25695–25704.